A NUMERICAL INVESTIGATION OF THE COMPRESSIBLE FLOW FIELD PRODUCED IN AN ANNULAR JET, CLOSE-COUPLED, GAS METAL ATOMIZER

Pedro I. Espina[†], Ugo Piomelli[*], and George E. Mattingly[‡]

[†,‡] *National Institute of Standards and Technology, Gaithersburg, Maryland 20899*
[*] *University of Maryland, College Park, Maryland 20742*

Abstract

The gas-only flow field produced by an annular jet, close-coupled, gas-metal atomizer is studied using numerical solutions of the compressible, Navier-Stokes equations. An adaptive grid scheme is used to improve accuracy and convergence rate. The simulation is validated by comparison with flow visualization and pressure measurements conducted in a configuration similar to the modeled one. The structure of the flow field is related to the geometrical parameters of the atomization nozzle assembly, and criteria for the detection of adverse atomization conditions are obtained from the numerical results.

[†] Mechanical Engineer, Fluid Flow Group
[*] Assistant Professor, Department of Mechanical Engineering
[‡] Leader, Fluid Flow Group

Introduction

The interaction between a high-speed gas flow and a liquid metal stream that occurs in gas-metal atomizers is a problem of major technological importance, because it determines the size and shape of the metal particles produced. Optimally, atomized powders have a unique microstructure which enables the production of parts with improved chemical and physical properties when compared with conventionally-cast parts.

Although the study of the full interaction between the gas and the liquid phases is beyond the present capabilities of computational techniques, a numerical calculation of the gas flow in the region preceding the gas-liquid interaction is nonetheless useful. Data resulting from such studies can give insight into the geometric configuration and flow parameters (plenum pressure, temperature etc.) most likely to yield the desired flow pattern in the interaction region. Correlation of the computational results with experiments is then required to relate the flow topology to the particle size and shape distributions of the metal powder produced.

This work documents a numerical study of the gas flow, which was computed by solving the laminar Navier-Stokes equations in a number of geometrical atomizer configurations. The study was carried out for close-coupled, annular jet atomization-nozzle assemblies. The geometrical and operational parameters were selected to match those used in experimental studies performed using an actual atomization nozzle assembly. Calculations were performed on a CRAY Y-MP 2/216 at the National Institute of Standards and Technology (NIST) in Gaithersburg, Maryland.

In the next section, the mathematical model used will be presented and the numerical method will be described. Then, the results of the numerical simulations will be presented. Finally, some general conclusions will be drawn, together with their implications for optimizing the metal powder production process.

Mathematical Formulation

In this section, the numerical approach utilized for the simulations of the gas flow fields will be discused first. Then, a brief description of the grid refindment scheme utilized will be given. Finally, the physical domain considered, as well as the boundary conditions applied to it, will be described.

Numerical Approach

The governing equations of the compressible, viscous flow of a gas are the Navier-Stokes equations, which, can be written in dimensionless vector form[1] as

$$\frac{\partial Q}{\partial t} + \frac{\partial F_j}{\partial X_j} = \frac{1}{Re}\frac{\partial G_j}{\partial X_j}, \tag{1}$$

where $Q = (\rho, \rho u_i, E)^T$ is the dependent variable vector contaning the conservation vari-

[1] Velocities are made dimensionless by the freestream speed of sound a_∞, pressure by $\rho_\infty a_\infty^2$, all other quantities are normalized using their freestream values (indicated by a subscript ∞). Lengths are made dimensionless by an arbitrary nominal length $x_o = 25.4\ mm$.

ables, and the inviscid flux vector, F_j, and the viscous flux vector, G_j, are defined as

$$F_j = \begin{pmatrix} \rho u_j \\ \rho u_i u_j + P\ \delta_{ij} \\ (E+P)u_j \end{pmatrix}, \quad G_j = \begin{pmatrix} 0 \\ \tau_{ij} \\ u_k \tau_{jk} - q_j \end{pmatrix}; \tag{2}$$

where ρ is the fluid density, u_i is the velocity component in the X_i direction, p is the pressure, δ_{ij} is the Kronecker delta, $i,j = 1,2$ [2] (for two dimensional and axisymetric systems), and E is the total energy per unit volume:

$$E = \rho\left(e + \frac{1}{2}u_k u_k\right), \tag{3}$$

where

$$e = p/\rho(\gamma - 1), \tag{4}$$

γ is the specific heat ratio for a thermally- and calorically-perfect gas. The viscous stresses are given by

$$\tau_{ij} = \mu\left(\frac{\partial u_i}{\partial X_j} + \frac{\partial u_j}{\partial X_i}\right) + \lambda\ \frac{\partial u_i}{\partial X_i}\ \delta_{ij}, \tag{5}$$

where μ and λ are the first and second coefficients of viscosity, respectively. Sutherland's law is used to obtain the viscosity as a function of temperature, T. The Reynolds number is $Re = a_\infty x_o/\nu_\infty$, where ν is the kinematic viscosity. The heat flux vector is

$$q_j = -\frac{K}{\beta_r Pr}\frac{\partial T}{\partial X_j}, \tag{6}$$

where K is the thermal conductivity, $\beta_r = a_\infty^2/C_{p\infty}T_\infty$ (where C_p is the specific heat at constant pressure), and the Prandtl number is defined as $Pr = C_{p\infty}\mu_\infty/K_\infty$. In the present study, both inviscid calculations (in which the viscous stresses and the heat flux are neglected to yield the Euler equations), and viscous solutions were performed.

If the system (1) is transformed into a curvilinear coordinate system $\xi_j = \xi_j(X_i)$, it can be written as

$$\frac{\partial \widehat{Q}}{\partial t} + \frac{\partial \widehat{F}_j}{\partial \xi_j} = \frac{1}{Re}\frac{\partial G}{\partial \xi_j}, \tag{7}$$

with

$$\widehat{Q} = \frac{1}{J}Q,\ \widehat{F}_j = \frac{1}{J}\left(\frac{\partial \xi_j}{\partial t}Q + \frac{\partial \xi_j}{\partial X_k}F_k\right),\ \widehat{G}_j = \frac{1}{J}\frac{\partial \xi_j}{\partial X_k}G_k \tag{8}$$

where J is the Jacobian of the transformation.

Solution of (7) is accomplished using the PARC code [1], based on the ARC2D algorithm [2]. In this algorithm the time advancement is performed using a backward Euler scheme, and flux splitting is used to linearize the flux terms. Approximate factorization is used to facilitate solution of the resulting equation and central difference discretization of the resulting equation yields a block pentadiagonal system which can be solved directly by Gauss elimination. Both second- and fourth-order artificial dissipation are introduced to suppress dispersion errors near shocks

[2] When indicial notation is used, summation over repeated indices is implied.

Adaptive Grid

The distribution of grid points throughout the computational domain will affect the accuracy of the numerical solution. The artificial dissipation introduced by the numerical scheme tends to smear discontinuities in the flow field (i.e., shock waves) over a finite number of grid cells. This in turn, will produce weaker spatial gradients of the flow properties in the numerical solution.

One way to reduce the errors due to an improper grid distribution is to relocate the grid points, in the computational domain, based on an initial solution computed using an unoptimized grid, and then generating a new grid based on the spatial distribution of a selected flow property. The new grid will have a high point density in areas of the flow field where sharp gradients are present, and more sparse point distributions in areas where the flow is relatively smooth. Once an improved grid is generated, the solution obtained using the initial grid is interpolated into the newly generated grid and the governing equations are advanced in time until a new steady-state is reached. The procedure is then repeated anew until the regridding procedure does not change the mesh any more.

The grid-adaptation technique used here is based on variational principles, and was developed by Gnoffo [3] and Nakahashi and Deiwert [4]. The implementation of this method by Davies and Venkatapathy [5] was used in this work.

Physical Domain and Boundary Conditions

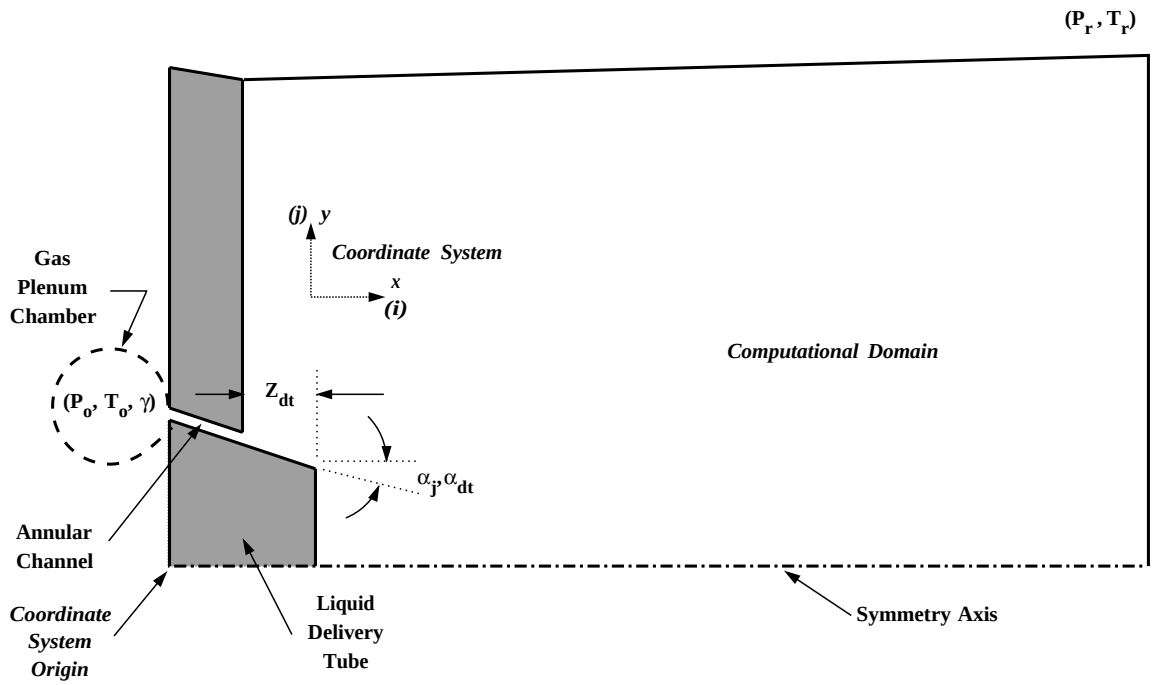

Figure 1. Schematic of azimuthal section of atomization nozzle assembly.

The geometry of the atomization nozzle assembly (or atomization die) examined and the relevant nomenclature are shown in Figure 1. The flow was assumed to be axisymmetric. The flow in the annular channel extending from the gas plenum chamber to the beginning of the delivery tube was calculated to obtain realistic velocity, density and pressure profiles at the exit point where the wall jet begins its flow along the conical liquid delivery tube.

The walls were assumed to be adiabatic, and no-slip conditions were imposed on the solid surfaces. At the inlet of the annular channel section, the stagnation pressure and temperature of the gas plenum chamber were imposed. Along subsonic surfaces at the end boundary of the computational domain, the static temperature and pressure were assigned, while over supersonic surfaces all quantities were extrapolated from upstream.

Results

Although a variety of flow configurations were studied, initial grids similar to that shown in Figure 2 were used for the discretization of the governing equations. This grid contains 25×25 points in the annular channel section, 24×43 in the section over the liquid delivery tube, and 136×73 points in the far field section. For cases in which the liquid delivery tube extension was reduced, the number of points over the delivery tube section (in the x-direction) was reduced to maintain the same initial Δx as in all other grids. The points subtracted from the delivery tube section were added to the far field section, keeping the overall number of points in the grid constant. In general, the distribution of points in the initial grid was constant both in the x and y directions. An exception was made in the y direction distribution over the delivery tube and in the far field, where the distribution of points was stretched to reflect the lack of significant flow phenomena in these areas. The initial grids did not affect the final results of the numerical simulations, since numerous adaptation cycles were performed before convergence was attained.

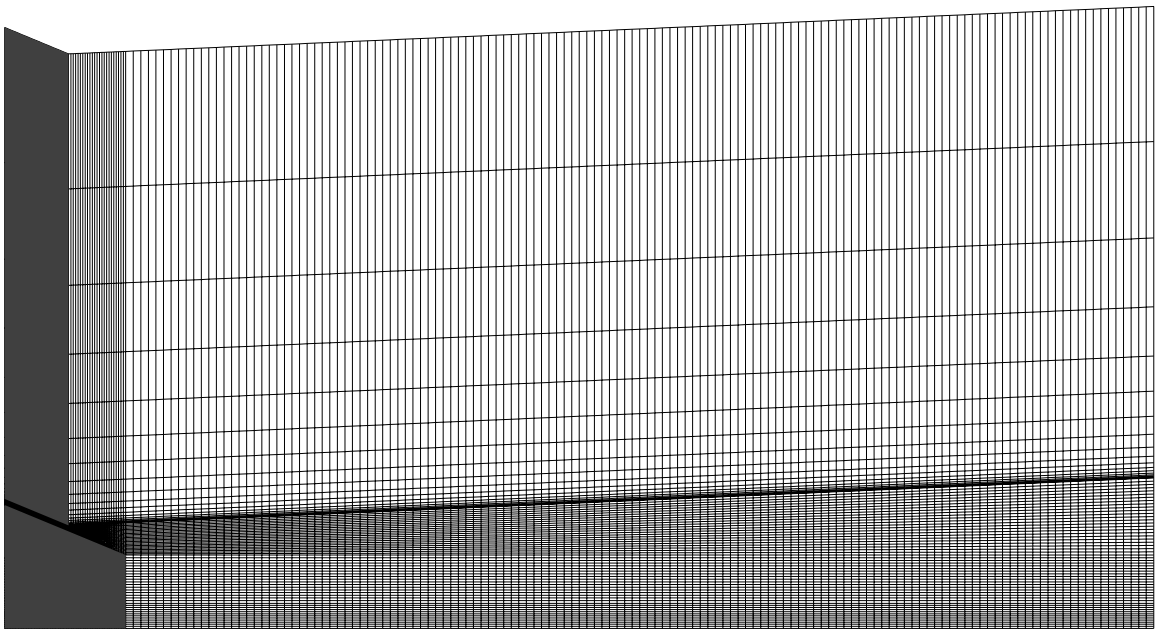

Figure 2. Initial grid distribution.[1]

To assess the validity of the simulations, the flow parameters were chosen to match those of the experiments carried out using the real atomization nozzle assembly [6, 7]. The reference pressure and temperature were $P_{ref} = 101.4\ kPa$ and $T_{ref} = 273.3\ ^{o}K$, while the receiving chamber pressure and temperature were $P_r = P_{ref}$ and $T_r = 1.0725\ T_{ref}$. The gas plenum chamber temperature was $T_r = 1.0725\ T_{ref}$. The liquid delivery tube extension, Z_{dt}, was varied in the experiments from a minimum of $0.054\ x_o$ to a maximum of $0.112\ x_o$.

[1] Circular arcs in the figure are a printing artefact, and should be ignored.

In the rest of this section, the effects of grid adaptation and viscosity on the numerical results will be discussed. Then, the flow field for the standard operational parameters will be described in detail. Finally, the flow field dependency on the liquid delivery tube length will be assessed.

Inviscid Solution – Effect of Grid Adaptation

When a grid distribution such as the one shown in Figure 2 is used to compute an inviscid solution of the gas flow produced in an atomizer, the numerical simulation yields a flow field with poorly resolved shear layers and smeared shock waves. To generate a better solution, the grid was adapted several times before negligible changes occurred in the flow field between successive adaptations. After each adaptation, the solution obtained using the old grid was used as the initial condition for the integration of the solution to a new steady state using the new grid. The numerical relaxation to obtain the steady state flow field was carried out until the change in the static pressure distribution was less than 1% of the previous value.

Figure 3 displays the final grid after the iterative process of relaxation-adaptation had been repeated about five times. The grid in the figure, which is a transformation of the grid in Figure 2, reveals heavy concentrations of points in areas of the flow field containing boundary layers, free shear layers, expansion fans, shock waves, and recirculation cells. The grid is significantly coarser in the far field, where the flow is nearly uniform.

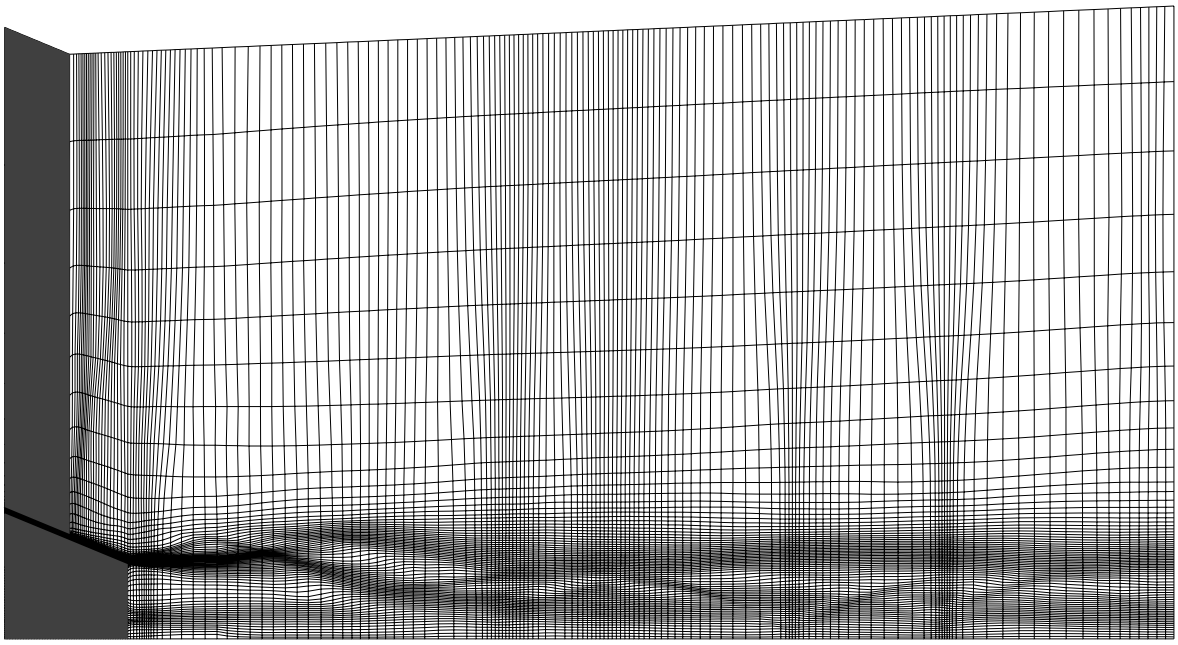

Figure 3. Final grid distribution showing an optimized arrangement of the mesh points to better resolve the flow structures in the jet produced at a pressure ratio, $P_o/\gamma P_{ref} = 37$ and $Z_{dt} = 0.112\ x_o$.

The evolution of the grid from its original unadapted distribution (seen in Figure 2) to its final adapted configuration (seen in Figure 3) considerably effects the results of the numerical simulations. Figure 4 compares the static pressure distributions along the axis of symmetry of the jet, before and after the relaxation-adaptation process. The static pressure on the axis of symmetry of the jet is made dimensionless by γP_{ref}. The line at

$P_r^* = P_r/\gamma P_{ref} = 1/\gamma$ is also shown to clarify the location of over-pressure and under-pressure regions within the jet.

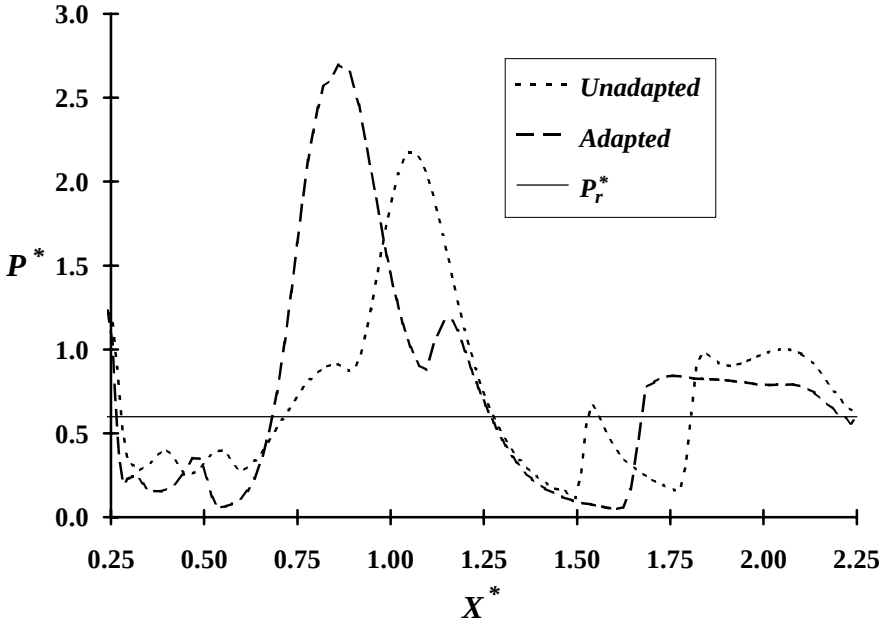

Figure 4. Effect of grid adaptation on the axial pressure distribution ($P_o/\gamma P_{ref} = 37$ and $Z_{dt} = 0.112\ x_o$).

The unadapted grid yields a pressure distribution which has a major peak in the vicinity of $X^* \approx 1.1$, and displays two minor peaks in pressure (at $X^* \approx 1.5$ and 1.8), which are typically associated with the presence of Mach reflections (i.e., normal shocks). In contrast, the distribution obtained in the adapted grid peaks in the neighborhood of $X^* \approx 0.86$, at a higher pressure than in the unadapted grid case. The first minor peak in pressure has moved upstream, to $X^* \approx 1.2$, and it has partially merged with the major pressure peak. The second minor pressure peak now stands alone at $X^* \approx 1.65$, and its magnitude has decreased from the one seen in the unadapted solution. The interpretation of these results is perhaps more clearly seen in terms of pressure changes through these shock structures.

For the unadapted case the pressure rise to the major peak is $\Delta P^* \approx 1.9$ while after grid adaptation this difference is $\Delta P^* \approx 2.6$. As noted above, the grid adaptation moves this flow feature upstream. However, for the first minor peak in the unadapted solution, the adaptation effect has merged this peak with the major peak. This obscures the observation that the pressure rise is enhanced by adaptation; although it is apparent that it is moved upstream. The second minor peak in the unadapted solution has a pressure rise that is duplicated in the adapted solution while being displaced upstream.

It appears, therefore, that grid adaptation produces a sharpening of flow gradient effect that generally elevates pressure peaks and pressure differences across shock structures. It also moves these features upstream in the flow field. These results are due to the fact that, in these supersonic flows, improvements in solution accuracy achieved by grid adaptation lead to improved upstream flow features and these, in turn, lead to improved downstream features. Although no quantitative comparisons have yet been completed using experimental pressure surveys, the flow fields obtained using grid adaptation compare better with Schlieren images than the solutions using unadapted grids, [6].

Viscous Solution

The inviscid solution described above was used as an initial condition, and the full equations (including the viscous stresses and heat flux term) were then integrated. Figure 5 displays the computed axial pressure distribution for viscous and inviscid flow; the inviscid solution is termed Euler and the viscous solution is labeled *Laminar*. For the laminar solution ($Re_{x_o} = 6.5 \times 10^5$), the major pressure peak is situated downstream of its original position; furthermore, the first minor pressure peak has merged with the main pressure peak. This made the initial pressure peak broader, and decreased its maximum value slightly. The Mach reflection also moves downstream. As was the case with the main pressure peak, the magnitude of the discontinuity introduced by the Mach reflection has been reduced by almost 20%.

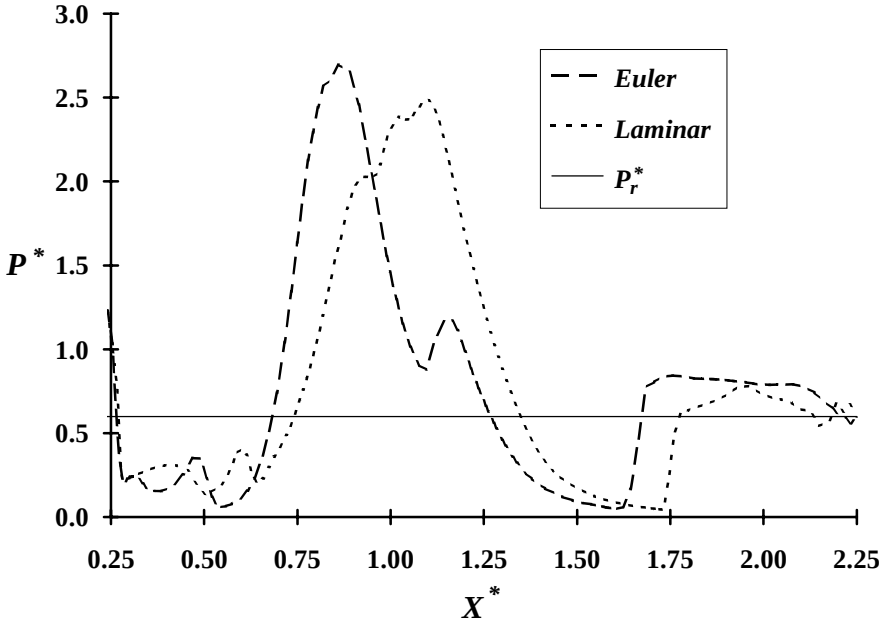

Figure 5. Effect of viscosity on the axial pressure distribution ($P_o/\gamma P_{ref} = 37.0$.)

Gas Only Flow Field Under Normal Operational Parameters

It is common industrial practice to operate gas atomizers under conditions which yield a maximum suction in the base region downstream of the end of the delivery tube. This maximum suction condition (also known as *maximum aspiration*) has been experimentally shown to yield the finest powder for a given atomizer [8]. Searching for a deeper understanding of the flow topology which yields the optimal metal powder product, simulations were carried out for the atomization jet operating at maximum aspiration.

For the atomizer geometry studied here, experiments [7] have shown that maximum aspiration is obtained for $Z_{dt} \approx 0.1\ x_o$ and $P_o/\gamma P_{ref} = 37$. Figure 6 displays the calculated Mach number distribution for these operating conditions. In this figure light gray denotes regions of high Mach number, while dark gray denotes regions of low Mach number.

Initially, the gas resides essentially at rest in the gas plenum chamber. From this chamber it exhausts through the annular channel (see Figure 1). By the end of the annular channel the flow has accelerated to sonic conditions (i.e., Mach number = 1) and it streams over the surface of the liquid delivery tube where, it forms an underexpanded wall jet. At the end of

the delivery tube the gas flow separates leaving a recirculation region trapped in the base region beyond the delivery tube. This recirculation region varies in extent along the axis of symmetry due to the expanding and contracting shapes of the two initial barrel shock cells (segment of a supersonic jet composed of expansion fans followed by compression shocks which has a shape similar to that of a rum barrel).

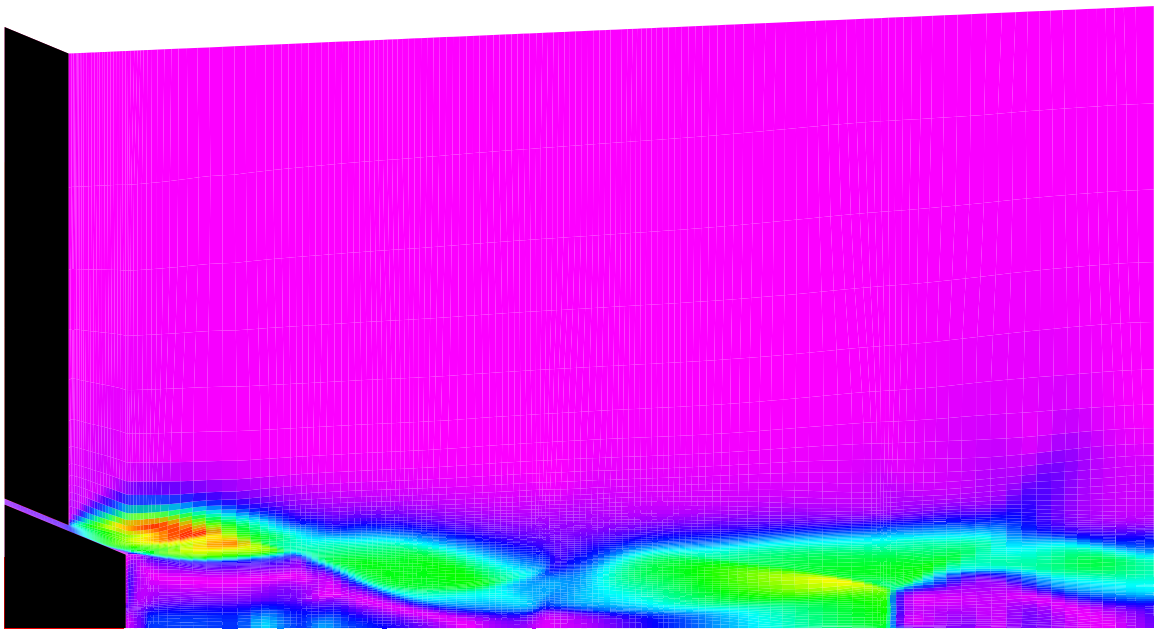

Figure 6. Mach number distribution for a pressure ratio, $P_o/\gamma P_{ref} = 37$, and $Z_{dt} = 0.112\ x_o$.

In the center of the first of these two barrel shocks the flow achieves its maximum Mach number of about 6. By the end of the second barrel shock the flow reaches the axis of symmetry of the jet, thereby enclosing the recirculating base flow. At this location an oblique shock wave is formed which satisfies the boundary condition imposed by the axis of symmetry (the flow straightens its trajectory to flow parallel to the axis of symmetry). The interaction between this oblique shock and the shocks at the end of the second barrel shock system generates the large pressure discontinuity at $X^* \approx 1.1$ seen in Figure 5. Downstream of this point the flow essentially loses its annular nature and effectively becomes a single jet. Within the first barrel shock structure of the newly formed single jet, the flow reflects from the axis of symmetry an incident oblique shock wave as a Mach reflection (normal shock structure towards the end of Figure 6). This normal shock decelerates the flow, forming a region of subsonic flow behind it (seen as the dark region at the right side of the figure). After this Mach reflection, the gas eventually accelerates to supersonic velocities and undergoes a succession of barrel shocks which eventually decelerate the flow to subsonic speeds.

Naturally most of this picture will change when liquid metal is present, but due to the supersonic nature of the jet some of these features will tend to remain in the annular region surrounding the liquid stream. The formation of the wall jet over the surface of the delivery tube can be expected to remain intact, given that the gas-liquid interaction takes place downstream of it. Furthermore, it can be hypothesized that most of the liquid flow will remain confined within the recirculating base region until it interacts with the gas flow at the major pressure peak (i.e., the discontinuity describe above). Of course, interactions will

occur along the shear layer which surrounds the liquid flow, but, with its high momentum, the gas jet should retain some of its features around the recirculation region (before the main pressure discontinuity). Evidence of this can be seen in the accumulation of liquid metal, within the base region at the end of the delivery tube that has been observed in high speed movies of the atomization process [6].

Finally, there is some qualitative agreement between the numerical results shown in Figure 6 and the Schlieren image of the real flow shown in Figure 7. In both images the existence of the predominant flow structures is apparent. To help clarify the flow structure in the Schlieren image the main features of the flow have been labeled in Figure 7.

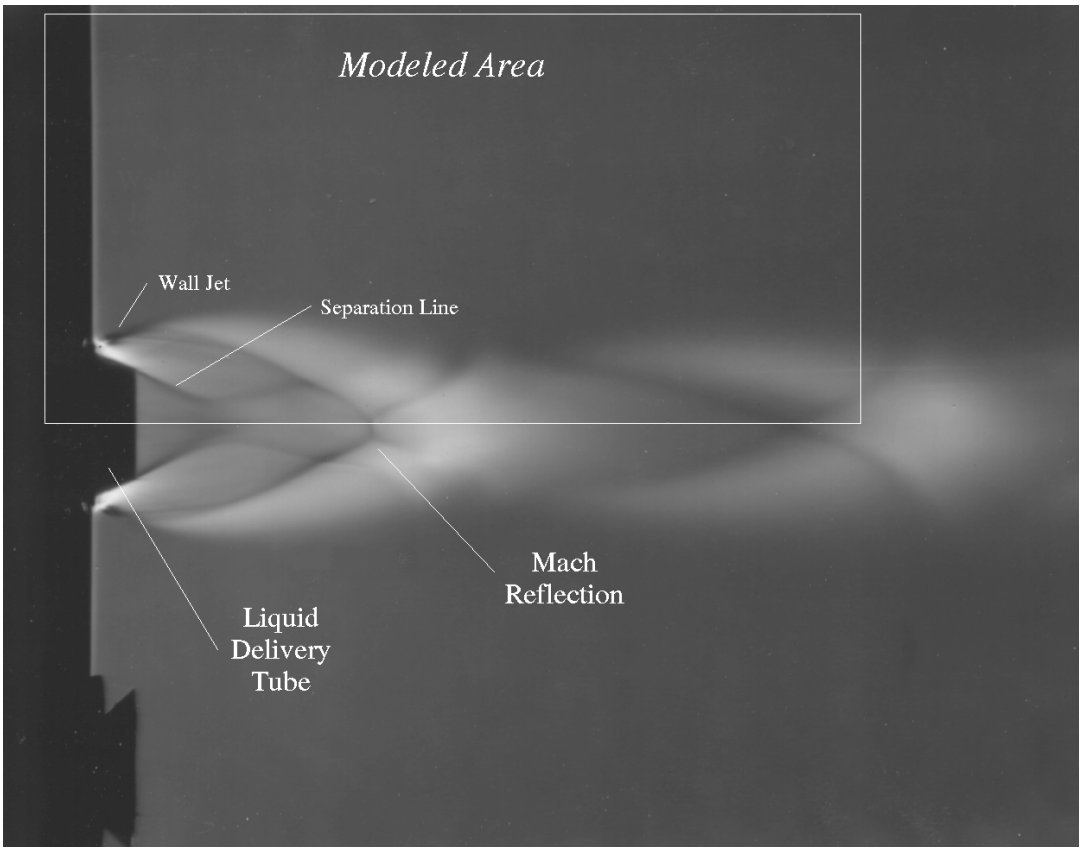

Figure 7. Schlieren photograph of the gas-only flow from an annular atomizer ($P_o/\gamma P_{ref} = 37$, and $Z_{dt} = 0.1\ x_o$).

Effect of Liquid Delivery Tube Length

The effect of the liquid delivery tube extension on the topology of the gas-only jets was studied. Three cases were examined, $Z_{dt} = 0.054,\ 0.087$, and $0.112\ x_o$, while all other parameters were held constant. Figure 8 compares the results obtained for these three cases.

As seen in the figure, for the longest delivery tube, the axial pressure distribution of this jet shows a region of relatively constant pressure associated with the recirculating base flow at the end of the delivery tube. Thereafter, the distribution peaks at $X^* \approx 1.1$ with a pressure of $P^* \approx 2.5$. The Mach reflection can be seen at $X^* \approx 1.75$, which causes a pressure recovery to exceed $P^* \approx 1.1$. For the medium-length delivery tube, the constant pressure section is followed by dual peaks in the pressure distribution with $P^* \approx 1.7$. Under these conditions the shocks at the end of the second barrel structure do not coincide in axial

location with the oblique shock formed on the axis of symmetry. This has the tendency of making the main pressure discontinuity broader. The Mach reflection moves upstream, and its intensity is increased. For the shortest liquid delivery tube, the major pressure peak is displaced downstream relative to that for the other cases. In this case, the shock waves at the end of the second barrel shock structures are further apart from the axial shock wave. As the result, the effect of the shocks at the end of the barrel shock structure are seen as the first mild peak in pressure at $X^* \approx 0.87$ and the presence of the axial shock can be seen in the maximum pressure peak at $X^* \approx 1.2$. The Mach reflection has moved further upstream, but it has decreased intensity.

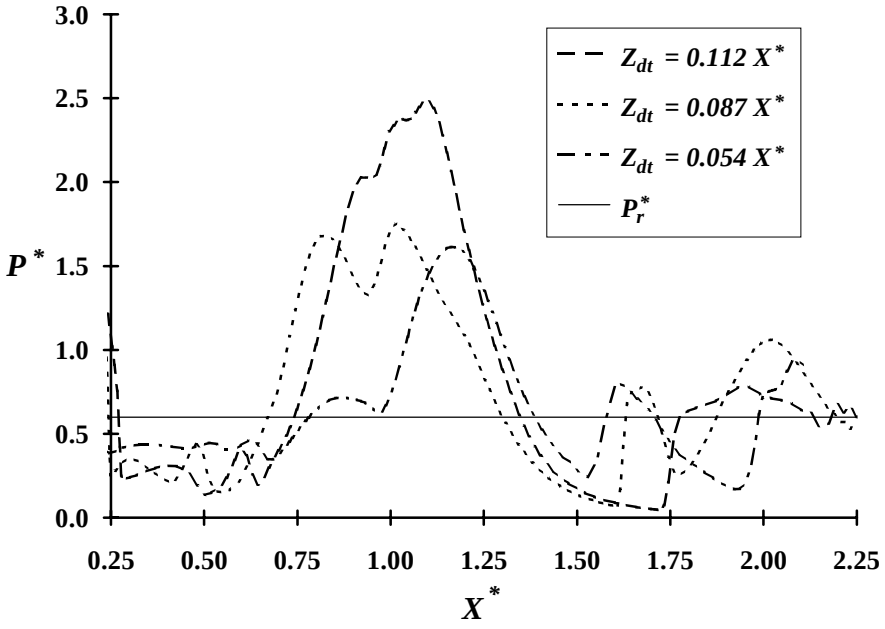

Figure 8. Effect of liquid delivery-tube extension on the axial pressure distribution (viscous solutions for $P_o/\gamma P_{ref} = 37$).

As Z_{dt} is increased, the pressure at the base of the liquid delivery tube decreases. This behavior is in agreement with experiments, as seen in Figure 9, which shows that the base pressure decreases with increasing liquid delivery-tube extension up to a value $Z_{dt,max}$, where the effect is reversed [7]. The value $Z_{dt,max}$ is a function of jet pressure ratio, for a given geometry and gas specie. For $P_o/\gamma P_{ref} = 37$ experiments indicate $Z_{dt,max} \approx 0.1\ x_o$ (see Figure 9). The structure of the flow field over the delivery tube surface helps explain this change in behavior.

Figure 10 shows the typical flow field over the face of the liquid delivery tube, for $Z_{dt} > Z_{dt,max}$. The gas remains attached to the surface of the delivery tube up to $Z_{dt} \approx Z_{dt,max}$, and then separates to form a recirculation region over the final stage of the liquid delivery tube. This recirculation region increases the pressure at the end of the liquid delivery tube, which, in turn, increases the base pressure, as observed in the experiments (see Figure 9). When the liquid delivery tube is shorter than $Z_{dt,max}$ the flow does not separate, and the base pressure is not affected by the formation of the separated flow region.

This flow separation occurs as the result of an adverse pressure gradient near the end of the liquid delivery tube that may produce a reversed flow of liquid metal on the face of the delivery tube. Given that the gas flow in this region has temperatures in the range

of 50 to 100°K, any flow of liquid metal onto this surface of the delivery tube will freeze and attach itself to the surface. This build-up will deteriorate the external geometry of the liquid delivery tube and degrade the aerodynamic conditions necessary for continuous atomization, finally resulting in a disastrous freeze-off.

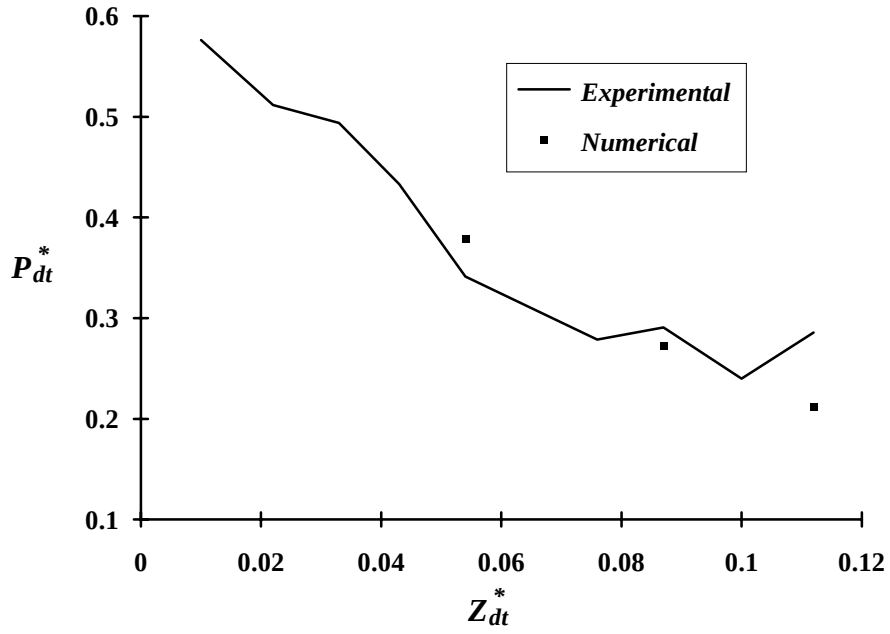

Figure 9. Comparison between numerical and experimental results for the aspiration pressure.

Figure 8 shows that for a constant pressure ratio $P_o/\gamma P_{ref}$, elongation of the liquid delivery tube extension increases the intensity of the axial pressure distribution maximum. This increase in the strength of the major pressure discontinuity could be responsible for the reported production of finer particles in atomizers with delivery tube extensions in the neighborhood of $Z_{dt,max}$ [8]. It is hypothesized that the presence of strong pressure discontinuities in the path of the liquid metal leads to enhancement of the liquid disruption process, which, in turn, yields finer particle size distributions.

Conclusions

The capability of an implicit, Reynolds-averaged Navier-Stokes solver for simulating the flow fields produced in a close-coupled, gas-metal atomizer has been demonstrated. The use of adaptive-grid algorithms has been shown to help resolve the position and intensity of the salient features of the flow structures contained in these processes. In addition the use of adaptive-grid techniques yielded improvements in convergence rate in these computationally expensive calculations. The numerical predictions of the aspiration pressure for different conditions are in good agreement with experimental data.

Elongated liquid delivery tube effects were shown to enhance the overall intensity of pressure discontinuities in the flow field. It is hypothesized that these strong pressure discontinuities in the flow field may intensify the liquid disruption dynamics during the metal-atomization process, leading to larger yields of smaller particles.

Extreme elongations of the liquid delivery tube were shown to produce adverse pressure gradients that resulted in separated flows. This separation can produce a reversed flow of

liquid metal onto the delivery tube surface detrimentally changing the gas flow characteristics and possibly deteriorating or terminating the atomization process.

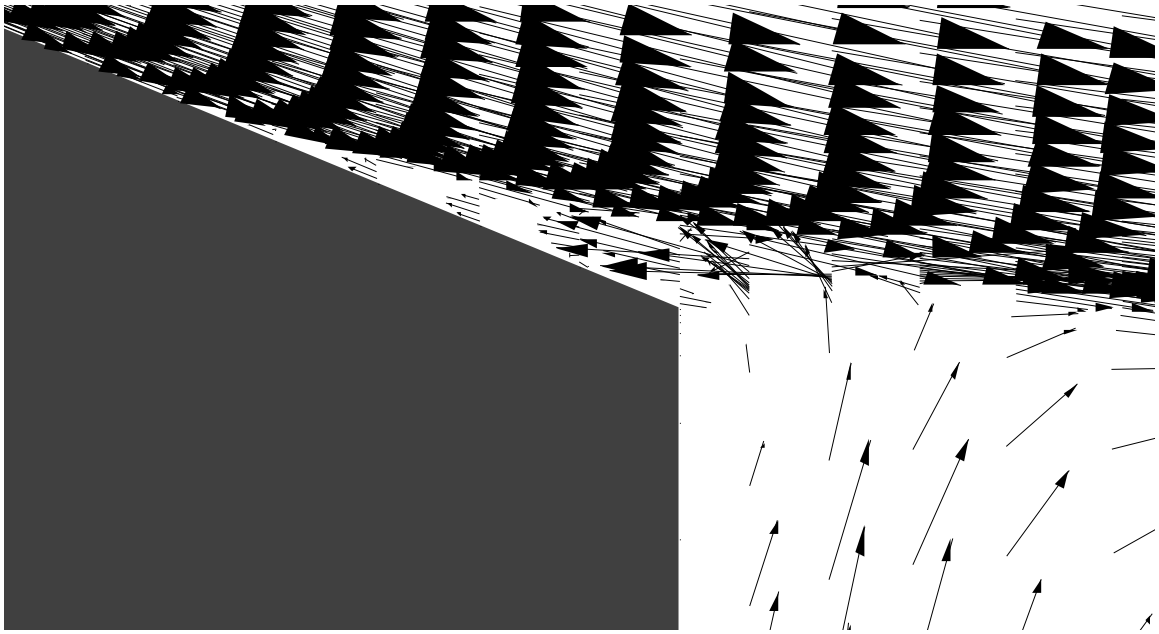

Figure 10. Detail of velocity distribution over the liquid delivery tube for $Z_{dt} = 0.112X^* > Z_{dt,max}$ and $P_o/\gamma P_{ref} = 37$.

Acknowledgments

This investigation was sponsored by the Office of Intelligent Processing of Materials of the National Institute of Standards and Technology and an industrial consortium between; Ampal/Metallurg, Flemington NJ; Crucible Materials Co., Pittsburgh, PA; DOE - Office of Industrial Processes, Washington, DC; General Electric Aircraft Engines, Lynn, MA; Martin Marietta, Oak Ridge, TN; and United Technologies - Pratt & Whitney, West Palm Beach, FL. Computational support was provided by the Computer Facilities Division of NIST.

References

[1] G. K. Cooper, "The PARC Code: Theory and Usage" (Report AEDC-TR-87-24, Arnold Engineering Development Center, 1983).

[2] T. H. Pulliam and J. L. Steger, "Implicit Finite-Difference Simulation of Three-Dimensional Compressible Flows," A.I.A.A. Journal, 18 (2) (1980), 159-167.

[3] P. A. Gnoffo, "A Finite-Volume, Adaptive Grid Algorithm Applied to Planetary Entry Flowfields," A.I.A.A. Journal, 21 (9) (1983), 1249-1254.

[4] K. Nakahashi and G. S. Deiwert, "Self-Adaptive-Grid Method with Application to Airfoil Flow" (A.I.A.A. Paper, No. 91-1594, 1991).

[5] C. B. Davies and E. Venkatapathy, "Application of a Solution Adaptive Grid Scheme, SAGE, to Complex Three-Dimensional Flows," A.I.A.A. Journal, 25 (4) (1987), 513-520.

[6] Ridder, S. D., et. al., "Intelligent Control of Particle Size Distribution During Gas Atomization," International Journal of Powder Metallurgy, 28 (2) (1992), 133-147.

[7] P. I. Espina, "An Experimental Investigation of the Compressible Flow in a Close-Coupled Inert Gas Metal Atomizer" (M.S. thesis, University of Maryland, 1991).

[8] J. D. Ayers and I. E. Anderson. "Very Fine Metal Powders," Journal of Metals, 37 (A) (1985), 16-21.